Journal of
Materials Chemistry B

Accepted Manuscript

ROYAL SOCIETY
OF CHEMISTRY

www.rsc.org/materialsB

A general top-down approach to synthesize rare earth doped-Gd_2O_3 nanocrystals as dualmodal contrast agents

Ningqi Luo[†,#], Chuan Yang[‡,#], Xiumei Tian[§], Jun Xiao[†], Jun Liu[†], Fei Chen[†], Donghui Zhang[†], Dekang Xu[†], Yueli Zhang[†], Guowei Yang[†], Dihu Chen[†,*], and Li Li[‡,*]

[†] State Key Laboratory of Optoelectronic Materials and Technologies, School of Physics & Engineering, Sun Yat-sen University, Guangzhou 510275, P. R. China

[‡] State Key Laboratory of Oncology in South China, Imaging Diagnosis and Interventional Center, Sun Yat-sen University Cancer Center, Guangzhou 510060, P. R. China

[§] Department of Biomedical Engineering, Guangzhou Medical University, Guangzhou 510182, P. R. China

[#] Authors contributed equally to this work.

[*] Corresponding authors. E-mail: stscdh@mail.sysu.edu.cn, li2@mail.sysu.edu.cn.

Abstract

Dualmodal contrast agents of rare earth doped gadolinium oxide (Gd_2O_3) nanoparticles with high spatial resolution for magnetic resonance imaging (MRI) and high sensitivity for fluorescence imaging have attracted intensive attention in biomedical imaging. However, the rare earth doped nanoparticles mentioned above have been so far synthesized by hydrothermal method, which is a bottom-up method, requiring high purity chemical reagents, and relying on the availability of the respective precursors and strict reaction condition. Here, we propose a facile and environmentally friendly top-down technique to synthesize the rare earth doped-Gd_2O_3 nanocrystals at ambient environment. Using this approach, we synthesize a series of Tm^{3+}, Tb^{3+}, and Eu^{3+} doped-Gd_2O_3 nanoparticles colloids and observe strong blue, green, and red visible fluorescence from the as-synthesized nanoparticles colloids. Cell confocal microscope images show that these synthesized nanoparticles colloids are good fluorescence imaging contrast agents. Taking Gd_2O_3:Eu^{3+} nanoparticles as an example, we evaluate their performance in MRI *in vitro* and *in vivo*. These results indicate that the synthesized rare earth doped-Gd_2O_3 nanocrystals can be used as MRI and fluorescence imaging dualmodal contrast agents. The developed technique is expected to be a general, facile and environmentally friendly strategy towards synthesizing of rare earth doped nanoparticles for biomedical applications.

Keywords: Laser ablation in liquid, Gd_2O_3:Tm^{3+}/Tb^{3+}/Eu^{3+}, nanoparticles colloids, fluorescence, magnetic resonance imaging.

1. Introduction

Dualmodal contrast agents with combining magnetic resonance imaging (MRI) and fluorescence imaging play an indispensable role in modern biomedical imaging.[1–4] Imaging techniques are irreplaceable tools in cancer research, clinical trials and medical practice.[5–7] Among the high-developed molecular imaging methods,[8] MRI and fluorescence imaging attract much attention.[3,8,9] MRI is an non-invasive technique, which provides a high spatial resolution of 50 μm, much higher than that of optical technique (1-2 mm).[10,11] Together with its good soft-tissue contrast, excellent perception with tomographic capabilities, and outstanding anatomical detail and orientation, MRI has already become one of the most important tools in medical image diagnostics.[11–13] However, its sensitivity is about 10^{-9}-10^{-6} moles of label detected, which is relatively lower than that of optical technique (whose sensitivity is higher up to 10^{-12} moles of label detected).[10] Dualmodal contrast agents combining MRI and fluorescence imaging offer high spatial resolution and high sensitivity, have thus attracted intensive attention in biomedical imaging.[14,15,9,16]

Gadolinium oxide (Gd_2O_3) is considered to be a promising candidate of T_1-weighted MRI contrast agent compared to the commercial clinical Gd-DTPA.[17–20] It is known that the key parameter of T_1-weighted contrast agents, the longitudinal relativity (r_1), is proportional to the number of water molecules that coordinate to the unpaired electrons of Gd^{3+}.[21] Gd_2O_3 whose surface Gd^{3+} offers all its seven unpaired electrons for water hydration resulting in larger r_1 values than that of Gd-DTPA. Gd-DTPA only offers one hydrate position since its other six unpaired electrons are coordinated by chelates. Therefore, researches are focusing on the synthesis of Gd_2O_3 particles for use as T_1-weighted MRI contrast agents.[22–24] Concerning fluorescence imaging contrast agents, rare earth doped nanoparticles are promising for biological applications due to their optical properties and low cytotoxicity, compared to the organic dyes, semiconductor fluorescent nanocrystals, or quantum dots.[25] Attractive properties of rare earth doped nanoparticles include high photostability, absence of blinking, extremely narrow emission lines, large Stokes shifts, etc. Thus, the rare earth doped Gd_2O_3 nanoparticles will be suitable dualmodal contrast agents to combine MRI and fluorescence imaging.

Traditionally, the rare earth doped nanoparticles are synthesized by hydrothermal method,[26] which is a bottom-up methods, requiring high purity chemical reagents, relying on the availability of the respective precursors and strict reaction condition. Here in this paper, we synthesize the rare earth doped Gd_2O_3 nanoparticles by a simple and facile approach of laser ablation in liquid (LAL). In recent years, LAL technology has attracted increasing attention in preparation of nanoparticles for all kinds of applications.[27,28] In LAL, nanoparticles are produced by focusing a pulsed-laser onto a bulk target immersed in a liquid solution. Compared to common chemical reductions or precipitation routes, its advantages can be summarized as follows: (i) Pollution free. LAL does not necessarily require chemicals and does not necessarily produce waste.[29,30] (ii) Purity. The whole process is carried out in pure deionized water, and chemical precursors and other chemicals are not required, the synthesized colloid is 100% pure and the nanoparticles are ligand-free. These ligand-free nanoparticles, whose surface are not blocked by the chemical ligands or residues of the reducing agents, possess high surface activity,[31] which leads to significant advantages for quality-demanding nanotechnology applications in biomedicine.[32] (iii) Facile. The LAL apparatus is apparently simple (Supplementary Fig. S1). It requires just a laser source and a liquid container with the submerged target where the laser beam is focused. Features, such as manual operation and the experimental setup are minimal, chemical precursors are replaced by bulk materials, make LAL facilitate the batch-to-batch and the lab-to-lab reproducibility of the synthesis and the biocompatibility of the products.[30] (iv) Versatility. Independent of the respective precursors, LAL allows for the production of nanoparticles from any base material (metal, alloy, semiconductor, and ceramic) and in numerous liquids. Since the pioneer work reported by Patil *et al.* in 1987,[33] LAL technology has been applied to synthesize a variety of nanomaterials in recent years.[28,34,27,35]

In this contribution, we combine LAL and standard solid state reaction techniques to synthesize the rare earth doped Gd_2O_3 nanoparticles. We firstly prepare solid targets (Tm^{3+}, Tb^{3+}, Eu^{3+} doped Gd_2O_3 solid targets) for laser ablation by pressing commercially available powders, and then ablate solid targets in liquid by a microsecond laser. Fluorescence properties of the synthesized nanoparticles are studied while their confocal microscope images of RAW264.7 cells are observed. Taking Gd_2O_3:Eu^{3+} as an example, we systemically characterize the morphology, structure, and component of the synthesized nanoparticles. Meanwhile, *in vitro* and *in vivo* MRI is evaluated. Furthermore, toxicity is evaluated by cell viability of RAW264.7, S18, and PC12 cell. Our investigations show that combing standard solid state reaction and LAL is a promising approach to synthesize rare earth doped nanoparticles for biomedical applications.

2. Methods and materials

Targets and Nanoparticles Preparation.

The rare earth doped Gd_2O_3 targets were prepared via a standard solid state reaction techniques. Gd_2O_3 and rare earth oxides (Tm_2O_3, Tb_2O_3, and Eu_2O_3) of analytical grade with an stoichiometric ratio of 95:5 were milled in a agate mortar for 30min. Polyvinyl alcohol (PVA, 7 wt%) solution was added into the powders as a binder, after which the powders were dried under 50℃ for 10min and sieved by a 60 mesh filter. The obtained powders were then uniaxially pressed into cylinders of 15mm in diameter under 15MPa. Sintering was performed at 1500℃ for 10h in air after a heating rate of 10℃/min. Targets were collected after the oven temperature natural cooled down.

The LAL apparatus has been reported in our previous work.[36] As shown in Fig. S1(a), rare earth doped Gd_2O_3 target was firstly fixed on the bottom of a container, and then deionized water was added into the chamber until the target was covered by 5 mm deionized water. A microsecond laser of Nd:YAG with a wavelength of 1064nm, 6μs pulse duration, a repetition of 100Hz, and power of 70 mJ/pulse, was focused onto the target surface. The ablation process lasted for 15 min. The ablated colloids were aged for 24 hours, and then the upper clear liquid were collected and centrifuged at 12000rpm for 15 min.

The mechanism of nanoparticles formation can be divided into two processes:[36–38] (i) Active species ejection: As shown in Fig. S1(b), after energy absorption of the focused laser beam, the target will eject high temperature active species of the same component as the target itself. (ii) Nanoparticles formation: the active species travel to their nearby area by difussion[39–41] and combine with each other, meanwhile their temperature decrease as result of the liquid confinement, and finally nanoparticles form. As shown in Fig. S1(c).

Samples Characterization.

Transmission electron microscope (TEM, FEI Tecnai G2 Spirit), X-ray diffractometer (XRD, D-MAX2200 VPC), and X-ray photoelectron spectrometer (XPS, ESCALab250) were employed to characterize the morphology, structure, and component of the products, respectively. The visible fluorescence images were taken by a digital camera under laser excitation of the nanoparticles colloid, while the fluorescence spectra were measured by Edinburgh spectrofluorophotometer (FLS920) at room temperature. The Gd^{3+} ion concentration was determined by inductively coupled plasma atomic emission spectroscopy (ICP-AES).

Cell Culture and *in Vitro* Confocal Microscope Imaging.

The RAW264.7 cells were maintained at 37°C under 5 % CO_2 in Dulbecco's modified Eagle's medium (DMEM) containing 10% fetal bovine serum (FBS), penicillin (100 units/ml), and streptomycin (100mg/ml). The cells were incubated with the Gd_2O_3:Tm^{3+}/Tb^{3+}/Eu^{3+} nanoparticles for 2h. After co-incubation, the cells were washed with PBS to remove the remaining particles and dead cells, and then observed under Confocal Microscope (ZEISS LSM 710), operating at 405nm excitation wavelength.

In Vitro MRI and Calculation of Longitudinal Relaxivity (r_1).

In vitro T_1-weighted MRI and longitudinal relaxivity value (r_1, unit of $s^{-1}mM^{-1}$) of the Gd_2O_3:Eu^{3+} were evaluated by a 3.0T Siemens Trio MRI scanner (Siemens Medical Solutions, Erlangen, Germany). The r_1 was calculated according to the equation $r_1 = \Delta R_1 / [Gd^{3+} concentration]$,[21] where R_1 was the longitudinal relaxation rate ($R_1 = 1/T_1$, unit of s^{-1}). In this study, R_1 of Gd^{3+} with different concentration (0-0.05mM) were measured with inversion recovery pulse sequences with T_R=3000 ms and T_I=500-2500 ms (17 measurement points). T_I was fitted to an exponential T_1 recovery model by a non-linear least square regression equation $S_{IR}(T_I) = S_0[1 - 2\exp(-T_I / T_1) + \exp(-T_R / T_1)]$, by which, R_1 $(1/T_1)$ of different Gd^{3+} concentration were determined.[42–44]

Cells Cytotoxicity.

In vitro cytotoxicity were evaluated using 3-(4,5-dimethylthiazol-2-yl)-2,5 diphenyltetrazolium bromide (MTT) assays. The RAW264.7, S18, and PC12 cells were employed to test the cytotoxicity of the Gd_2O_3:Eu^{3+} nanocrystals. Cells in 96-well plates were cultured at 37℃, 5% CO_2 with different concentrations of the Gd_2O_3:Eu^{3+} nanocrystals (10 μM, 1 μM and 100 nM) for 48 h, compared with negative control (culture media, DMEM) and positive control (lipopolysaccharide, LPS). After the incubation, 20 µL of MTT was added, the cells were incubated for another 4 h. Then all the culture medium was removed, and 100 µL dimethyl sulfoxide (DMSO) was added to each well to dissolve the formazan crystals for 10 min. The absorbance at 490 nm was measured by a microplate reader (Bio-Rad, USA).

Animal Model and *In Vivo* MRI.

Animal experiments were done according to the National Institutes of Health guidelines on the rules of animals during research. Four to six-week-old Balb/c nude mice (weight of 18 to 22 g) were bought from the animal experiment center of the Medical College, Sun Yat-sen University, China, and maintained in a specific pathogen-free (SPF) environment (Certificate No. 26-99S031). Mice were subcutaneously injected with 5 × 106 nasopharyngeal carcinoma (NPC) CNE-2 cells with 100 µL phosphate buffered saline (PBS).Ten days after tumor cell inoculation, mice were randomized by tumor size (approximately 60 mm^3). Following induced anesthesia by intraperitoneal injection of 0.1% mebumalnatrium (10 mL per g weight) mice were injected via the tail vein with 15 µ mol kg^{-1} of the Gd_2O_3:Eu^{3+} in 100 mL of 0.4% carboxymethylcellulose sodium and transported to the 3.0 T Siemens Trio MRI scanner, using a surface coil constructed specically for small animals (3 inch in diameter).

3. Results and discussion

Visible blue, green, and red fluorescence of Gd_2O_3:Tm^{3+}, Gd_2O_3:Tb^{3+}, and Gd_2O_3:Eu^{3+} nanoparticles colloids are showed in Fig. 1(a). These pictures are recorded by a digital camera without using any optical filters when the nanoparicles colloids are excited by 275nm laser. The bright visible fluorescence indicate that Tm^{3+}, Tb^{3+}, and Eu^{3+} have been successfully doped into the

Gd_2O_3, since only the rare earth doped Gd_2O_3 materials give fluorescence emission (Supplementary Fig. S2 (a)). Taking $Gd_2O_3:Eu^{3+}$ for example, we notice that none of the Gd_2O_3 and Eu_2O_3 mixture, Eu_3O_3 colloid, Gd_2O_3 colloid, or background deionized water exist these emission properties (Supplementary Fig. S2 (b)-(e)). It is during the solid state reaction process that the rare earth doped into Gd_2O_3, and the LAL preparation of related nanoparticle does not change its fluorescence property, as the target shows the sample emission spectrum as the nanoparticle does (Supplementary Fig. S2 (f)). The LAL plays a role of preparing nanoparticles from their bulk targets by a top-down way. By combining the standard solid state reaction technique to prepare targets with LAL to fabricate nanoparticles by the top-down way, it's a general approach to preparing rare earth doped Gd_2O_3 nanoparticles as well as other doped nanomaterials. The emission spectra shown in Fig. 1 (b) give high intensity of blue, green, and red peaks for $Gd_2O_3:Tm^{3+}$, $Gd_2O_3:Tb^{3+}$, and $Gd_2O_3:Eu^{3+}$ nanoparticles, respectively. Their energy transfer processes are described in Fig. 1 (c). Under 275nm excitation, photons are transferred from ground state $^8S_{7/2}$ to excited state ^6I_J. Then energy transfer occurs between Gd^{3+} and different activators (Tm^{3+}, Tb^{3+}, or Eu^{3+}) after the nonradiative energy decay from ^6I_J to ^6P_J. High energy states of different activators are unstable, which cause depopulation and subsequently decay nonradiatively to the excited states. Visible emissions will then occur from these states back to their relevant ground states.

To determine whether the rare earth doped Gd_2O_3 nanocrystals can be used as potential optical tags for cellular studies, we perform *in vitro* cells confocal microscope imaging using a Confocal Microscope (ZEISS LSM 710) operating at 405nm excitation wavelength. Fig. 2 (a), (d), and (g) show the bright-field images of RAW264.7 cells after 2 hours of incubation with the $Gd_2O_3:Tm^{3+}$, $Gd_2O_3:Tb^{3+}$, and $Gd_2O_3:Eu^{3+}$ nanoparticles, respectively. Obviously, the cells swallow the nanoparticles and the materials cause no significant damage to the cells. Figure 2 (b), (e), and (h) shows the fluorescence images of blue, green, and red of Gd_2O_3:Tm^{3+}, Gd_2O_3:Tb^{3+}, and Gd_2O_3:Eu^{3+} nanoparticles inside the cells matrix, respectively. They show that the materials possess high fluorescence emission properties even after swallowing by the cells. The merge figures shown in Fig. 2 (c), (f), and (i) give the intracellular fluorescence, which indicate that the S18 cells have taken up Gd_2O_3:Tm^{3+}, Gd_2O_3:Tb^{3+}, and Gd_2O_3:Eu^{3+} nanoparticles through the specific immunoglobulin recognition, confirming the samples can be used as potential fluorescence imaging contrast agents. However, to use these nanoparticles *in vivo*, more experiments are needed to evaluate their performances.

We take Gd_2O_3:Eu^{3+} nanoparticles for example to characterize their properties for use as dualmodal contrast agents. Detailed morphological information of the sample is characterized by TEM. A typical TEM image (Fig. 3 (a)) shows these nanoparticles obtain good dispersibility. Though these nanoparticles are not modified by any chemical ligands, their surfaces are charged and thus obtain an extremely high colloidal stability.[31,36,45] The corresponding size distribution histogram shows the mean size of the nanoparticles is 7.4nm. As shown in Fig. 3 (b) the HRTEM, the interplanar distance of Gd_2O_3:Eu^{3+} nanocrystal is about 0.310nm, which is in good agreement with that of Gd_2O_3 in the database (d_{111} = 0.316nm, PDF#42-1465). Further XRD measurement is carried out to determine the structure of the sample. As shown in Fig. 3 (c), the XRD pattern of Gd_2O_3:Eu^{3+} is in good agreement with the PDF#42-1465 for Gd_2O_3, suggesting that the slight Eu-doping doesn't change the monoclinic structure of Gd_2O_3. The peaks are strong and narrow, indicating the good crystallinity of the samples. The components of the products are characterized by XPS. As shown in Fig. 3 (d), peaks at 1220.5eV, 1188.5eV, and 1135.0eV denote $Gd3d_{3/2}$, $Gd3d_{5/2}$, and $Eu3d_{5/2}$, respectively. The peak positions are consistent with the energy level for Gd in Gd_2O_3[46] and Eu in Eu_2O_3,[47] thus verifying the valence state of the elements in the sample.

To explore the potential of using $Gd_2O_3:Eu^{3+}$ nanocrystals as T_1-weighted MRI contrast agents, MRI measurement is carried out by a 3.0T Siemens Trio MRI scanner. In vitro MR images in Fig. 4 (a) show a series of T_1-weighted MR images with different Gd^{3+} concentration, compared to the commercial clinical MRI contrast agent Gd-DTPA. As the Gd^{3+} concentration increase, the nanoparticles brightened the MR images, which suggest that they act as T_1-weighted MRI contrast agents. For the same Gd ion concentration, the MR image containing the nanoparticles is much brighter than that containing Gd-DTPA, indicating $Gd_2O_3:Eu^{3+}$ obtains a better MRI enhancement than Gd-DTPA. The r_1 value is measured to understand its effectiveness from a quantitative perspective. As shown in Fig. 4 (b), $Gd_2O_3:Eu^{3+}$ obtain a much higher r_1 value of $34.26 s^{-1}mM^{-1}$ than that of Gd-DTPA ($4.22\ s^{-1}mM^{-1}$). Based on the Solomon-Bloembergen-Morgan (SBM) theory, a classical theory for interpreting relaxation of water protons in the presence of a contrast agent,[48–50] water proton relaxation has a $1/r^6$ dependence on the distance between the Gd^{3+} ion and water protons. It means that the shorter the distance between the surface Gd^{3+} ion and water proton is, the higher the relaxivity. It has been proved that the surface of the LAL synthesized nanoparticles is not blocked by any chemical ligands or residues of any reducing agents,[51] which reduce the distance between Gd^{3+} ion and water proton. We suggest the high relativity of these LAL synthesized nanoparticles is resulted from their ligand-free surface which ensure the distance between water proton and surface Gd^{3+} ion is small enough.

To evaluate the biocompatibility of the $Gd_2O_3:Eu^{3+}$ nanocrystals, RAW264.7, S18, and PC12 cells are employed to test the cytotoxicity of the products. The cell viability remains above 90%

(Supplementary Fig. S3) for all cells of difference nanoparticles concentration after co-incubation of the cells and the nanoparticles for 48 hours, which suggests that the nanoparticles cause no significant cytotoxic effect in the long term. No significant difference between $Gd_2O_3:Eu^{3+}$ nanocrystals and Gd-DTPA is found. The good crystallinity of the nanoparticles (judging from the XRD shown in Fig. 3 (c)) confines the Gd^{3+} in rigid matrices, which makes it hard to release, resulting in the low toxicity of the nanoparticles.[32,52]

Finally, in vivo MRI is measured. The 3.0T T_1-weighted MR images of a NPC CNE-2 xenografted tumor are showed in Fig. 4 (c), which clearly show a high contrast enhancement of the tumor after injecting the $Gd_2O_3:Eu^{3+}$ nanocrystals (15 μmol kg^{-1}) at 35 minutes (Fig. 4(d)). These in vivo MR images results indicate the nanoparticles to be good T_1-weighted MRI contrast agents for biomedical applications.

4. Conclusions

In summary, we have developed a general top-down strategy to synthesize the rare earth doped Gd_2O_3 nanocrystals for use as dualmodal contrast agents by combining standard solid state reaction and LAL. Tm^{3+}, Tb^{3+}, and Eu^{3+} doped Gd_2O_3 nanoparticles were synthesized, and strong blue, green, and red visible fluorescence emissions were observed from the products. Taking $Gd_2O_3:Eu^{3+}$ nanoparticles as an example, we characterized the morphology, structure, and component of the synthesized nanoparticles, and found out that the products were excellent dispersibility and good crystallinity. The measurements showed that they can be used as efficient fluorescence imaging and MRI contrast agents. According to the cell viability results, $Gd_2O_3:Eu^{3+}$ nanoparticles cause no significant cytotoxic effect. Further *in vivo* MRI showed the nanoparticles to be good T_1-weighted MRI contrast agents for biomedical applications. These investigations provided a general, facile and simple approach to synthesis rare earth doped nanoparticles of great potential in biomedical applications.

Acknowledgments

This work was supported by the National Basic Research Program of China (2014CB931700) and the National Natural Science Foundation of China under Grant No. 81071264, 61071039, and 81271622, and 81071207, the Project Science and Technology of Guangdong Province (2011A090200037).

Notes and references

Supporting Information is available free of charge via the Internet at http://pubs.rsc.org.

1. R. Toy, E. Hayden, A. Camann, Z. Berman, P. Vicente, E. Tran, J. Meyers, J. Pansky, P. M. Peiris, H. Wu, A. Exner, D. Wilson, K. B. Ghaghada, and E. Karathanasis, *ACS Nano*, 2013, **7**, 3118–29.
2. O. Veiseh, C. Sun, J. Gunn, N. Kohler, P. Gabikian, D. Lee, N. Bhattarai, R. Ellenbogen, R. Sze, A. Hallahan, J. Olson, and M. Zhang, *Nano Lett.*, 2005, **5**, 1003–8.
3. N. Biodistribution, S. Kunjachan, F. Gremse, B. Theek, P. Koczera, R. Pola, M. Pechar, T. Etrych, K. Ulbrich, G. Storm, F. Kiessling, and T. Lammers, *ACSNano*, 2013, **7**, 252–262.
4. L. E. Jennings and N. J. Long, *Chem. Commun. (Camb).*, 2009, 3511–24.
5. R. Weissleder and M. J. Pittet, *Nature*, 2008, **452**, 580–9.
6. F. Erogbogbo, K. Yong, I. Roy, R. Hu, W. Law, W. Zhao, H. Ding, F. Wu, R. Kumar, M. T. Swihart, and P. N. Prasad, *ACSNano*, 2011, **5**, 413–423.
7. S. P. Foy, R. L. Manthe, S. T. Foy, S. Dimitrijevic, N. Krishnamurthy, and V. Labhasetwar, *ACSNano*, 2010, **4**, 5217–5224.
8. S. Achilefu, *Chem. Rev.*, 2010, **110**, 2575–8.
9. R. Kumar, M. Nyk, T. Y. Ohulchanskyy, C. A. Flask, and P. N. Prasad, *Adv. Funct. Mater.*, 2009, **19**, 853–859.

10. M. Baker, *Nature*, 2010, **463**, 977–980.

11. E. Terreno, D. D. Castelli, A. Viale, and S. Aime, *Chem. Rev.*, 2010, **110**, 3019–42.

12. K. N. Raymond and V. C. Pierre, *Bioconjugate chem.*, 2005, **16**, 3–8.

13. P.-C. Wu, C.-H. Su, F.-Y. Cheng, J.-C. Weng, J.-H. Chen, T. Tsai, C.-S. Yeh, W.-C. Su, J. R. Hwu, Y. Tzeng, and D.-B. Shieh, *Bioconjugate chem.*, 2008, **19**, 1972–1979.

14. S. a. Corr, Y. P. Rakovich, and Y. K. Gun'ko, *Nanoscale Res. Lett.*, 2008, **3**, 87–104.

15. A. Louie, *Chem. Rev.*, 2010, **110**, 3146–95.

16. J. Zhou, Y. Sun, X. Du, L. Xiong, H. Hu, and F. Li, *Biomaterials*, 2010, **31**, 3287–95.

17. X.-H. Ma, A. Gong, L.-C. Xiang, T.-X. Chen, Y.-X. Gao, X.-J. Liang, Z.-Y. Shen, and A.-G. Wu, *J. Mater. Chem. B*, 2013, **1**, 3419.

18. H. K. Cho, H.-J. Cho, S. Lone, D.-D. Kim, J. H. Yeum, and I. W. Cheong, *J. Mater. Chem.*, 2011, **21**, 15486.

19. Ja Young Park, M. J. Baek, E. S. Choi, S. Woo, J. H. Kim, T. J. Kim, J. C. Jung, K. S. Chae, Y. Chang, G. H. Lee, L. Relaxivity, O. Particle, J. Y. Park, and S. Chae, *ACS Nano*, 2009, **3**, 3663–3669.

20. C. H. Reynolds, N. Annan, K. Beshah, J. H. Huber, S. H. Shaber, R. E. Lenkinski, and J. A. Wortman, *J. Am. Chem. Soc.*, 2000, **122**, 8940–8945.

21. P. Caravan, *Chem. Soc. Rev.*, 2006, **35**, 512–23.

22. H. K. Cho, H.-J. Cho, S. Lone, D.-D. Kim, J. H. Yeum, and I. W. Cheong, *J. Mater. Chem.*, 2011, **21**, 15486.

23. A. Tiwari, D. Terada, P. K. Sharma, V. Parashar, C. Yoshikawa, A. C. Pandey, and H. Kobayashi, *Anal. Methods*, 2011, **3**, 217.

24. J.-L. Bridot, A.-C. Faure, S. Laurent, C. Rivière, C. Billotey, B. Hiba, M. Janier, V. Josserand, J.-L. Coll, L. Vander Elst, R. Muller, S. Roux, P. Perriat, and O. Tillement, *J. Am. Chem. Soc.*, 2007, **129**, 5076–84.

25. C. Bouzigues, T. Gacoin, and A. Alexandrou, *ACS Nano*, 2011, 8488–8505.

26. H. Liu, L. Li, X.-M. Tian, W.-Y. Hu, X.-Y. Kuang, and Y.-Z. Shao, *Eur. J. Inorg. Chem.*, 2012, **2012**, 5677–5684.

27. H. Zeng, X.-W. Du, S. C. Singh, S. a. Kulinich, S. Yang, J. He, and W. Cai, *Adv. Funct. Mater.*, 2012, **22**, 1333–1353.

28. G. Yang, *Prog. Mater. Sci.*, 2007, **52**, 648–698.

29. V. Amendola and M. Meneghetti, *Phys. Chem. Chem. Phys.*, 2009, **11**, 3805–21.

30. V. Amendola and M. Meneghetti, *Phys. Chem. Chem. Phys.*, 2013, **15**, 3027–3046.

31. S. Barcikowski and G. Compagninib, *Phys. Chem. Chem. Phys.*, 2013, **15**, 3022–3026.

32. N. Luo, X. Tian, C. Yang, J. Xiao, W. Hu, D. Chen, and L. Li, *Phys. Chem. Chem. Phys.*, 2013, **15**, 12235–12240.

33. P. P. Patil, D. M. Phase, S. A. K. Kulkarni, S. V Ghaisas, S. M. Kanetkar, S. B. Ogale, V. G. Bhide, R. Quenching, and A. Oxidation, *Phys. Rev. Lett.*, 1987, **58**, 238–241.

34. G. Yang, *Laser Ablation in Liquids: Principles and Applications in the Preparation of Nanomaterials*, Pan Stanford Publishing Pte. Ltd., 2011.

35. Z. Yan and D. B. Chrisey, *J. Photoch. Photobio. C*, 2012, **13**, 204–223.

36. N. Luo, X. Tian, J. Xiao, W. Hu, C. Yang, L. Li, and D. Chen, *J. Appl. Phys.*, 2013, **113**, 164306.

37. K. Y. Niu, J. Yang, S. a Kulinich, J. Sun, H. Li, and X. W. Du, *J. Am. Chem. Soc.*, 2010, **132**, 9814–9.

38. C. X. Wang, P. Liu, H. Cui, and G. W. Yang, *Appl. Phys. Lett.*, 2005, **87**, 201913.

39. F. Mafuné, J. Kohno, Y. Takeda, T. Kondow, and H. Sawabe, *J. Phys. Chem. B*, 2000, **104**, 8333–8337.

40. F. Mafuné, J. Kohno, Y. Takeda, T. Kondow, H. Sawabe, and F. Mafune, *J. Phys. Chem. B*, 2000, **104**, 9111–9117.

41. F. Mafuné, J. Kohno, Y. Takeda, T. Kondow, H. Sawabe, and F. Mafune, *J. Phys. Chem. B*, 2001, **105**, 5114–5120.

42. P. Hou, K. M. Hasan, C. W. Sitton, J. S. Wolinsky, and P. a Narayana, *AJNR Am J Neuroradiol.*, 2005, **26**, 1432–8.

43. G. Liang, J. Ronald, Y. Chen, D. Ye, P. Pandit, M. L. Ma, B. Rutt, and J. Rao, *Angew. Chem.*, 2011, **123**, 6407–6410.

44. A. Klasson, M. Ahrén, E. Hellqvist, F. Söderlind, A. Rosén, P.-O. Käll, K. Uvdal, and M. Engström, *Contrast Media Mol. Imaging*, 2008, **3**, 106–11.

45. S. Barcikowski and F. Mafune, *J. Phys. Chem. C*, 2011, **115**, 4985–4985.

46. D. Raiser and J. P. Deville, *J. Electron Spectrosc.*, 1991, **57**, 91–97.

47. Y. Uwamino, T. Ishizuka, and H. Yamatera, *J. Electron Spectrosc. Relat. Phenom.*, 1984, **34**, 67–78.

48. I. Solomon, *Phys. Rev.*, 1955, **99**, 559–565.

49. N. Bloembergen, *J. Chem. Phys.*, 1957, **27**, 572.

50. N. Bloembergen and L. O. Morgan, *J. Chem. Phys.*, 1961, **34**, 842.

51. J. Xiao, X. M. Tian, C. Yang, P. Liu, N. Q. Luo, Y. Liang, H. B. Li, D. H. Chen, C. X. Wang, L. Li, and G. W. Yang, *Sci. Rep.*, 2013, **3**, 3424.

52. L. Zhou, Z. Gu, X. Liu, W. Yin, G. Tian, L. Yan, S. Jin, W. Ren, G. Xing, W. Li, X. Chang, Z. Hu, and Y. Zhao, *J. Mater. Chem.*, 2012, **22**, 966.

FIGURE CAPTIONS

Figure 1. Optical properties of Gd_2O_3: Tm^{3+}/Tb^{3+}/Eu^{3+} nanoparticles. (a) Fluorescence images of the as-prepared nanoparticles colloids in deionized water. These pictures, from left to right, Gd_2O_3: Tm^{3+}/Tb^{3+}/Eu^{3+}, with excitation laser wavelength of 275nm were taken with a digital camera without using blue, green, or red filters. (b) Emission spectra of Gd_2O_3: Tm^{3+}/Tb^{3+}/Eu^{3+} nanoparticles from left to right in colour of blue, green, and red respectively, on excitation wavelength of 275nm. (c) Illustration of energy transfer between sensitizer Gd^{3+} and different activators, Tm^{3+}, Tb^{3+}, and Eu^{3+}. Full arrows represent excitation and emission while the bold arrows stand for the naked eyes observed colour of the samples (consistent with (a)). Dotted arrows represent multiphonon relaxation. Curly arrows represent energy transfer.

Figure 2. Confocal microscope images of RAW264.7 cell incubated with Gd_2O_3:Tm^{3+}, Gd_2O_3:Tb^{3+}, and Gd_2O_3:Eu^{3+} nanoparticles, respectively. (a), (d) and (g) Bright-field images. (b), (e) and (h) Fluorescence images under 405nm wavelength excitation. (c), (f) and (i) Merged images.

Figure 3. Material characterization of Gd_2O_3:Eu^{3+} nanoparticles. (a) Typical TEM with size distribution histogram and SAD pattern as inset. (b) HRTEM of one particle with the interplanar distance of 0.310nm. (c) XRD pattern of synthesized nanoparticles compared to PDF#42-1465 of monoclinic Gd_2O_3. (d) Gd 3d and Eu 3d XPS spectra of Gd_2O_3:Eu^{3+} nanoparticles.

Figure 4. MRI evaluation of Gd_2O_3:Eu^{3+} nanoparticles. (a) *In vitro* T_1-weighted MR images of the

Gd_2O_3:Eu^{3+} compared to Gd-DTPA. (b) Plots of the relaxation rate ($1/T_1$) as a function of Gd^{3+} concentration, whose slopes provide the longitudinal relaxivity (r_1) of the contrast agents. (c) *In vivo* MRI color images of a NPC CNE-2 xenografted tumor before, 10min., 20min., 35min., 50min., and 70min. after Gd_2O_3:Eu^{3+} nanoparticles (15 μmol kg^{-1}) injection. (d) Signal intensity of the tumor changes with difference injection time of the nanoparticles, indicating the tumor get the best imaging enhancement at 35min. after the particles injection.

Figure 1

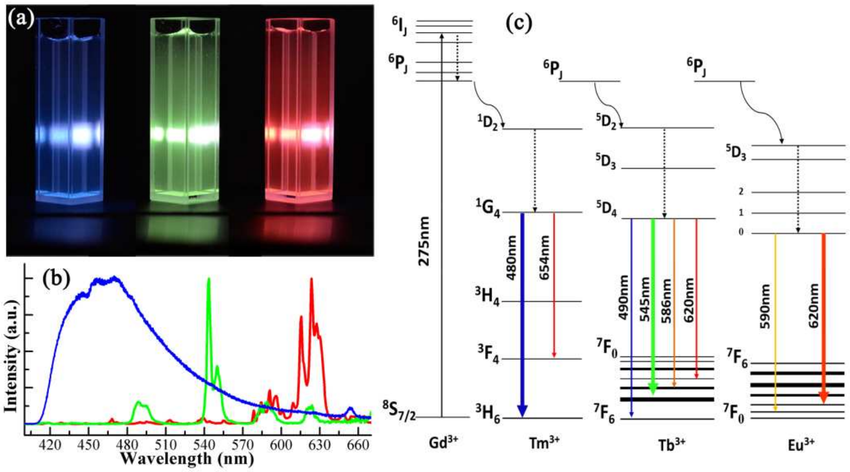

Figure 2

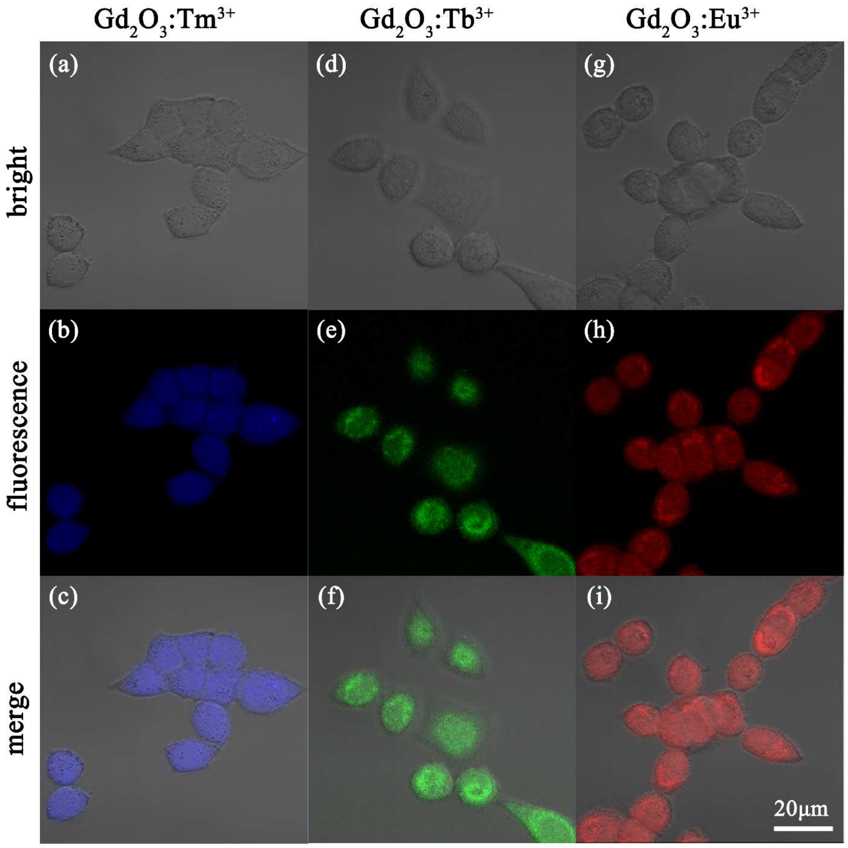

Figure 3

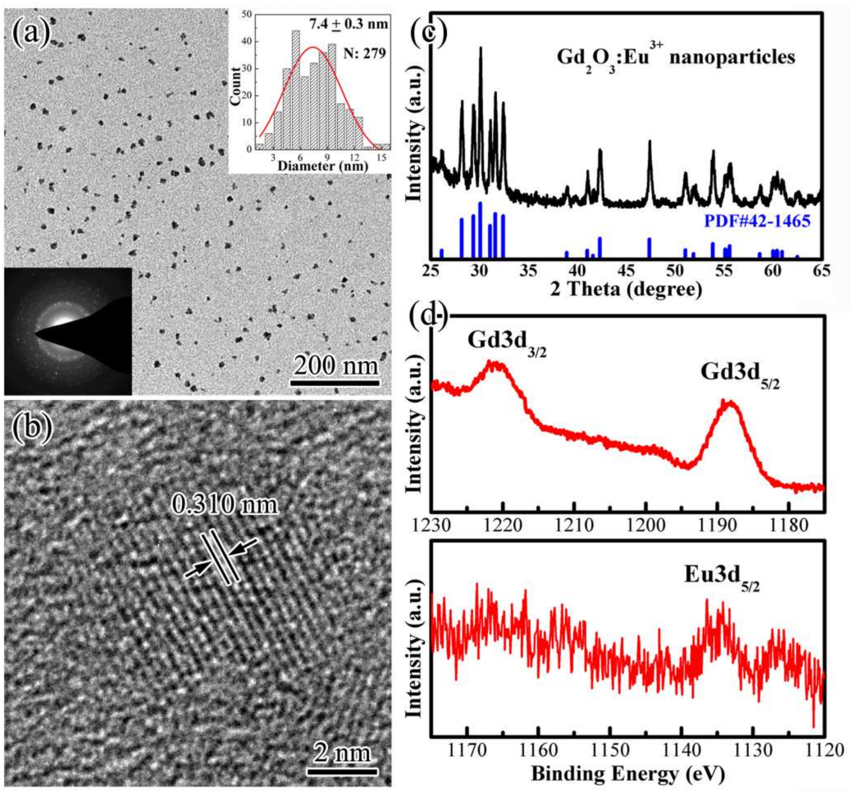

Figure 4